Materialia 21 (2022) 101323

Contents lists available at ScienceDirect

Materialia

journal homepage: www.elsevier.com/locate/mtla

Influence of B content on microstructure, phase composition and mechanical properties of CVD Ti(B,N) coatings

Michael Tkadletz[a,*], Nina Schalk[a,b], Alexandra Lechner[c], Lukas Hatzenbichler[a], David Holec[a], Christina Hofer[a], Marco Deluca[c], Bernhard Sartory[c], Andrey Lyapin[d], Jaakko Julin[e,f], Christoph Czettl[g]

[a] Department of Materials Science, Montanuniversität Leoben,Franz Josef-Straße 18, 8700 Leoben, Austria
[b] Christian Doppler Laboratory for Advanced Coated Cutting Tools at the Department of Materials Science, Montanuniversität Leoben, Franz-Josef-Straße 18, 8700 Leoben, Austria
[c] Materials Center Leoben Forschung GmbH, Roseggerstraße 12, 8700 Leoben, Austria
[d] Physical Electronics GmbH, Salzstraße 8, 85622 Feldkirchen bei München, Germany
[e] Helmholtz-Zentrum Dresden-Rossendorf, Institute of Ion Beam Physics and Materials Research, Bautzner Landstrasse 400, 01328 Dresden, Germany
[f] Department of Physics, University of Jyväskylä, P.O. Box 35, 40014 University of Jyväskylä, Finland
[g] CERATIZIT Austria GmbH, Metallwerk-Plansee-Straße 71, 6600 Reutte, Austria

ARTICLE INFO

Keywords:
Ti(B,N)
Chemical vapor deposition (CVD)
Borides
Atom probe tomography (APT)
Micromechanics

ABSTRACT

Within this work the effect of the B content on the microstructure, phase composition and mechanical properties of CVD Ti(B,N) coatings is investigated. Ti(B,N) coatings with B contents from 0 (fcc-TiN) to ~5, ~15, ~30, ~45 and 66 (h-TiB_2) at.% have been deposited by CVD. The elemental composition of the coatings was confirmed by ERDA and their microstructure was investigated using XRD and SEM. With increasing B content, a transition from a fcc to a h-dominated structure via dual-phase fcc/h-Ti(B,N) was observed, which was accompanied by a decreasing grain size from the µm to nm range. Combinatorial use of Raman spectroscopy, XPS and APT measurements indicated B-rich grain boundary segregations and the formation of increasing amounts of h-$Ti(B,N)_2$ clusters embedded within an fcc-Ti(B,N) matrix up to B contents of ~30 at.%, while for ~45 at.% B the matrix was predominantly composed of h-$Ti(B,N)_2$. Complementary ab initio calculations predicting the phase formation confirmed the interpretation of the experimental results. In terms of the mechanical properties, nanoindentation measurements and micromechanical testing revealed a rise in hardness from ~18 to ~41 GPa and an increasing fracture stress and toughness from ~7 to ~13 GPa and ~4.6 to ~5.5 $MPam^{1/2}$, respectively, by increasing the B content up to ~30 at.%. In contrast, a significant drop in hardness, fracture stress and fracture toughness was observed at ~45 at.% B. Thus it can be concluded, that both h-TiB_2 and dual-phase fcc/h-Ti(B,N) coatings with maximized B content yield superior properties over TiN and consequently improved performance.

1. Introduction

In recent years, a reviving interest in B containing chemically vapor deposited (CVD) hard coatings is reflected by an increasing number of publications covering binary, ternary as well as quaternary systems [1–9]. This might be due to the circumstance that representatives like TiB_2 usually perform well in demanding cutting applications [10], which can be related to its strong covalent bonding character and consequently superior mechanical properties like high hardness around 40–50 GPa [5,11]. Further, its inertness and thus low sticking tendency to Al which makes it a favorable candidate for machining Al and its alloys [12]. Further, CVD TiB_2 usually exhibits high in-plane compressive residual stress, which is generally favored for hard coatings, but rather exceptional for representatives deposited by thermally activated CVD [5].

However, direct deposition of TiB_2 onto cemented carbide tools using thermally activated CVD would lead to the formation of an unwanted CoWB compound at the interface [1,2]. This phase is known to deteriorate the mechanical properties of the substrate and consequently causes tool failure during application. Thus, CVD TiB_2 coatings typically comprise a TiN base-layer, which prevents B diffusion into the substrate [5,13]. However, this TiN/TiB_2 bi-layer architecture comes at a cost, since it causes a sharp transition from the face-centered cubic (fcc) TiN to the hexagonal (h) TiB_2 structure, causing a sudden change from tensile to compressive residual stress and pronounced differences in the me-

* Corresponding author at: Montanuniversität Leoben, Roseggerstrasse 12, 8700, Leoben, Austria.
E-mail address: michael.tkadletz@unileoben.ac.at (M. Tkadletz).

https://doi.org/10.1016/j.mtla.2022.101323
Received 4 January 2022; Accepted 9 January 2022
Available online 10 January 2022

chanical properties of both layers [5,6,13]. This negatively affects the adhesion of the TiB_2 on the TiN, which results in the need of a proper bonding strategy between TiN and TiB_2. Recently, works by Czettl et al. [13] and Tkadletz et al. [6] have shown that a gradual transition from TiN to TiB_2, by omitting a sharp transition and gradually increasing the B content, yields significant improvements in TiN-TiB_2 bonding. An alternative approach would be to completely avoid the pure TiB_2 by implementing ternary Ti(B,N) coatings instead, which potentially represent equivalent solutions.

Recent works confirm the feasibility of the industrial scale deposition of Ti(B,N) coatings by thermally activated CVD and indicate promising suitability for cutting applications [1,2,4,8]. The reported coatings mainly consisted of a dual-phase mixture of fcc-TiN and h-TiB_2, with indications for amorphous (a) TiB fractions at global B contents < 18 at.% [4]. However, while similar results were found within one of our previous investigations on a graded TiN-Ti(B,N)-TiB_2 coating [6], the diffraction and spectroscopy techniques applied so far do not allow for a thorough conclusion about chemical composition within the individual constituents. Thus, interdiffusion of B and N between the crystalline fcc-TiN and h-TiB_2 phases and consequent substitution of the one within the other is still not unambiguously clarified. In addition, besides the reported increase in hardness with increasing B content [1,2,6], the consequent influence on fracture stress and toughness of such coatings has not been systematically investigated. Existing studies on fracture properties of CVD Ti(B,N) based coatings mainly focused on samples with low B contents around ~5 at.% and respective multi-layer coatings with TiN as second component [7,8]. Thus, the dedicated goal of this work is to investigate the role of the B content on phase formation and the resulting mechanical properties of CVD Ti(B,N) coatings in order to establish a comprehensive understanding of the resulting microstructure - property relationships by applying a comprehensive portfolio of advanced characterization techniques.

2. Experimental details

All coatings investigated within this work were deposited onto SNUN 120,412 (ISO 1832) cemented carbide substrates with 11 wt.% Co, 12 wt.% mixed carbides and 77 wt.% WC using a SuCoTec SCT600 TH industrial scale CVD plant. $TiCl_4$, BCl_3, N_2, Ar and H_2 were used as precursors for the TiN, TiB_2 and Ti(B,N) coatings with aimed global B contents of ~5, ~15, ~30 and ~45 at.%. Similar to our previous study on a graded Ti(B,N) coating [6], the $BCl_3/TiCl_4$ ratios for each individual coating were adjusted accordingly, while the deposition temperature for all layers was kept within 860 to 920 °C at a pressure of 900 mbar. For the well-established TiN and TiN/TiB_2 coatings, a total thickness of ~4.5 µm was aimed (~1 µm TiN base-layer within TiN/TiB_2). While for the deposition of the Ti(B,N) coatings, a ~1.8 µm thick TiN base-layer was deposited to serve as diffusion barrier during further deposition, preventing B diffusion into the substrate. Subsequently, the deposition time of the Ti(B,N) coatings was kept constant at ~5 h, to evaluate the influence of the $BCl_3/TiCl_4$ ratio on the respective layer thickness and consequently the corresponding deposition rate. Further details on the deposition parameters of each individual layer can be found in ref. [13].

The elemental composition, especially with regard to the B content, of the Ti(B,N) coatings was determined utilizing elastic recoil detection analysis (ERDA) performed at the Helmholtz-Zentrum Dresden-Rossendorf using a 35 MeV $^{35}Cl^{7+}$ ion beam. The angle between the sample normal and the incoming beam was 75° degrees, the beam spot was approximately 1.5×1.5 mm^2. Recoiled sample atoms were detected using a Bragg ionization chamber placed at an angle of 31° with respect to the incoming beam. Scanning electron microscopy (SEM) investigations of the coating surfaces and cross-sections have been performed using a Zeiss Auriga cross-beam field emission SEM equipped with an Orsay Physics Cobra Z-05 focused ion beam (FIB) column. The X-ray diffraction (XRD) investigations were done using a Bruker D8 advance diffractometer, equipped with parallel beam optics (i.e. using a Goebel mirror and an equatorial Soller collimator of 0.12° opening). All measurements were performed in detector scan mode at an incidence angle of 2° using a step size of 0.02° and a counting time of 1.2 s within a 2θ range of 30–85° Raman spectra of the coatings were recorded using a HORIBA Jobin Yvon LabRAM 800 Raman spectrometer utilizing a green laser (λ=514.5 nm) operated at a power of 2 mW, focused through a 100x microscope objective (NA 0.8, Olympus). X-ray photoelectron spectroscopy (XPS) measurements were performed with a PHI Quantum 2000 spectrometer, equipped with a focused monochromatic Al-K_α (1486.68 eV) X-ray source operated at a power of 100 W using a beam footprint of $\sim 1.4 \times 0.4$ mm^2. Prior to the measurements, the sample surfaces were cleaned from any surface residues using an integrated Ar^+ ion beam operated at 1 kV using a beam footprint of $\sim 2 \times 2$ mm^2. Specimen (i.e. tips) for atom probe tomography (APT) were prepared via the lift-out technique [14], using a dual beam SEM/FIB of type FEI Versa 3D. Subsequently, at least two tips of each Ti(B,N) sample were investigated using a CAMECA LEAP 3000X HR operated at 60 K in laser assisted mode, applying a power of 0.4–0.6 nJ per pulse, a target evaporation rate of 0.50% and a pulse rate of 250 kHz. The measurements were evaluated using the CAMECA IVAS 3.6.14 software, at which an evaporation field of 40 V/nm according to ref. [15] was chosen for the 3D reconstruction of the datasets.

The mechanical properties of all samples were investigated using a Hysitron TriboIndenter TI950. For the investigation of hardness and Young´s modulus, quasi-static nanoindentation measurements on mechanically polished samples were performed using a diamond Berkovich indenter tip. At least 15 indents per sample, applying a maximum load of 10 mN (resulting in a penetration depth well below 10% of the coating thickness), were performed, and subsequently evaluated according to Oliver and Pharr [16]. For the evaluation of the corresponding fracture stress and fracture toughness, 5 notched and 5 unnotched microcantilevers ($\sim 3 \times 3 \times 9$ µm^3 in size) of each coating were prepared. The above described Zeiss Auriga cross-beam SEM/FIB was used applying decreasing beam currents down to 1 nA for the final cuts and 100 pA for the notch preparation resulting in a notch depth of ~550–650 nm. The same Hysitron TI950, but equipped with a cono-spherical diamond indenter tip (750 nm nominal tip radius), was used to load the prepared microcantilevers until fracture. Prior to loading, their corresponding loading point was aligned with the axis of the indenter using the built-in scanning probe microscopy feature. Afterwards, the collected data was analyzed according to the procedure described by Matoy et al. [17].

3. Results

3.1. Microstructure, chemical & phase composition

Surface and cross-section SEM images of the investigated coatings are shown in Fig. 1. While for the pure TiN a facetted surface topography can be identified, B addition immediately yields a distinct change towards a finer and less facetted topography with TiB_2 showing the smoothest surface of all investigated coatings. The Ti(B,N) coatings with moderate B content exhibit spike or needle-like features on their surface. This is in good agreement with the microstructures observed in the cross-sectional images, where TiN shows comparatively large columnar grains. Addition of B immediately results in a smaller grain size and seems to foster the growth of needle-shaped crystallites at low and intermediate B contents, as visible from the micrographs of the cross-sections. At higher B contents the grain size further decreases, the SEM cross-sections appear more and more featureless and the needle-shaped crystallites seem to disappear, which is in accordance with the observed surface topography, where surface spikes get less pronounced. For both, the single-layered TiN as well as the TiN/TiB_2 bi-layer coating, the aimed overall thickness of ~4.5 µm was obtained. Since the deposition rate of the Ti(B,N) coatings with different B contents was not exactly known, their deposition time was kept constant. Their resulting thickness reveals a strong effect of the B content, or more precisely of the $BCl_3/TiCl_4$ ratio,

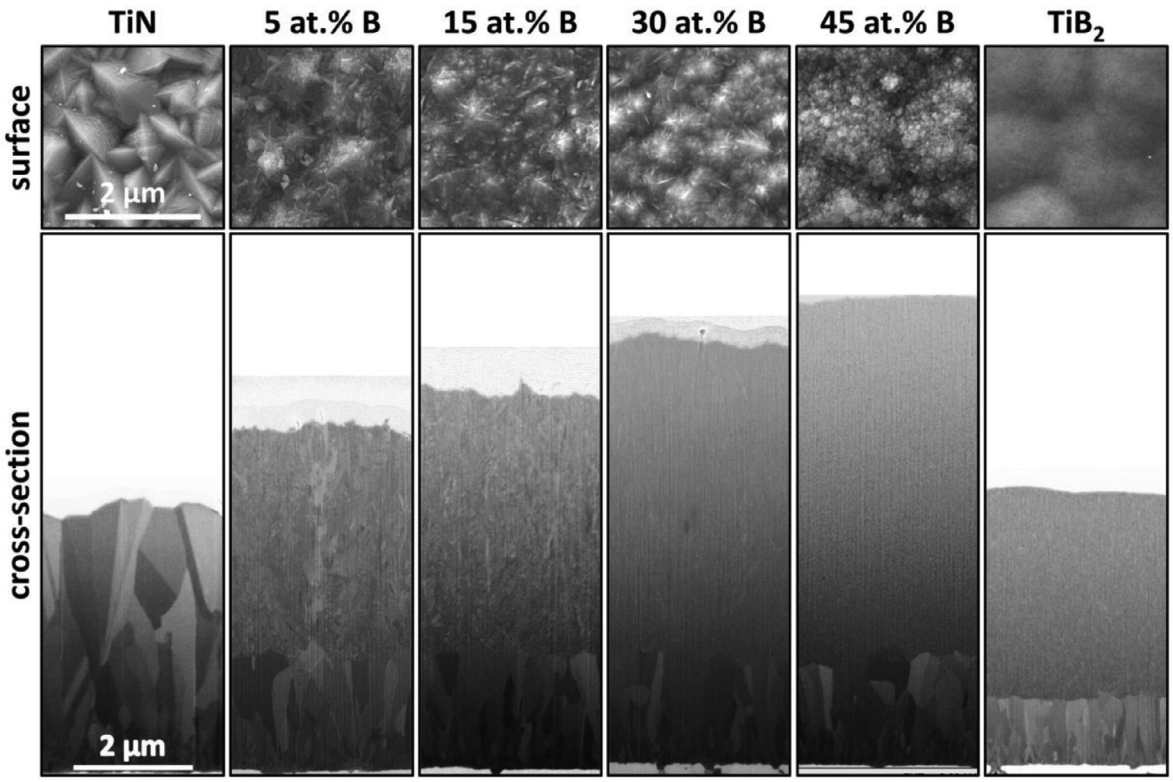

Fig. 1. Surface topography and cross-sectional SEM images of the investigated TiN, TiN/Ti(B,N) and TiN/TiB_2 coatings.

Table 1
Elemental composition of the respective Ti(B,N) samples determined via ERDA.

aimed B content [at.%]	Ti [at.%]	B [at.%]	N [at.%]
5	48.8 ± 1	5.7 ± 0.6	45.4 ± 1
15	46.5 ± 1	14.4 ± 1	39.1 ± 1
30	43.0 ± 1	29.3 ± 1	27.7 ± 1
45	36.1 ± 1	43.4 ± 1	20.3 ± 1

on the deposition rate. The thickness of the Ti(B,N) layers successively increases from ~3.8 µm (5 at.% B) to ~4.4 µm (15 at.% B), ~5.2 µm (30 at.% B) and finally ~6.0 µm (45 at.% B), yielding a rise in deposition rate from ~0.76 µm/h (5 at.% B) to ~1.20 µm/h (45 at.% B). In comparison, TiN and TiB_2 exhibit deposition rates of ~0.60 µm/h and ~1.00 µm/h, respectively. In contrast to the single-layer TiN coating and the TiN base-layers, the B containing coatings do not show any signs of competitive growth or increasing grain size with increasing coating thickness. Their small grain size and featureless appearance at high B contents is preserved throughout the whole coating thickness.

Results of the elemental composition of the Ti(B,N) coatings obtained by ERDA measurements are summarized in Table 1. An excellent agreement of the actually realized B contents with the aimed values is confirmed. Thus, for simplification, throughout this manuscript the Ti(B,N) coatings will be further referred to as by their aimed B contents of 5, 15, 30 and 45 at.% as already initiated in Fig. 1. The increase in B content is accompanied by a decrease of the N and Ti content. For the samples up to 30 at.% B, the observed ratios of Ti, B and N fit quite well to a mixture of either TiN and TiB_2 or TiB_xN_{1-x} and $Ti(B_xN_{1-x})_2$, while the Ti content at 45 at.% B does not fit into that scheme. There, the fractions of Ti and $(B + N)$ are already rather close to that of pure $Ti(B_xN_{1-x})_2$.

The XRD patterns of all samples are shown in Fig. 2a. Due to a significantly decreasing intensity with increasing B content, the scans were normalized to allow for a better qualitative comparison. For the TiN coating, as expected, a single-phase fcc structure is present. The peaks are rather narrow and appear at their expected standard peak positions (PDF 00–038–1420 [18]). Although the coating texture should be only discussed with caution, since the scans were performed in grazing incidence geometry, the 111 reflection appears to be the most prominent one, indicating a certain preferred orientation. With addition of B, the 111 reflection immediately gets less dominant and the peaks exhibit a distinct broadening which is indicative for a decreasing domain size and possibly increasing microstrains. In addition, the formation of the h-TiB_2 phase (PDF 00–035–0741 [18]) is already indicated for the lowest B content of 5 at.% and can be unambiguously identified for B contents higher than that. An evaluation of the lattice parameters of the corresponding phases with respect to the B content via Rietveld refinement revealed a more or less constant value of ~4.24 ± 0.01 Å for the fcc-phase, which is in perfect agreement with the lattice parameter of TiN, indicated in the powder diffraction file (PDF 00–038–1420 [18]). For the h-phase, the lattice parameter of the basal plane (a value) also stayed more or less constant and with 3.02 ± 0.02 Å again close to the tabulated value for TiB_2 given in the powder diffraction file (PDF 00–035–0741 [18]). The lattice parameter of the prismatic plane (c value) was with 3.58 ± 0.01 Å for the 15 at.% B sample higher than the tabulated one, and constantly decreased towards 3.44 ± 0.01 Å for 45 at.% B and finally 3.21 ± 0.01 Å for pure h-TiB_2 which is again in perfect agreement with the tabulated value. An estimation of the XRD domain sizes revealed a value of ≥ 1500 nm for the fcc-phase in pure TiN, which instantly deceased to ~27 ± 2 nm within the 5 at.% B sample and continuously further decreased to a value as low as ~3 ± 2 nm for the sample with 45 at.% B sample. A domain size of the h-phase of ~17 ± 5 nm was determined for the sample with 15 at.% B which decreased down to ~4 ± 1 nm for the 45 at.% B sample and yielded a final and slightly higher value of ~10 ± 1 nm for the pure h-TiB_2.

To complement the XRD investigations and to obtain information on the possible formation of amorphous compounds, Raman spectroscopy measurements were performed on the samples. Similar to the XRD measurements, the intensity decreased with increasing B content, which can be related to the decreasing grain size resulting in a reduced Raman effi-

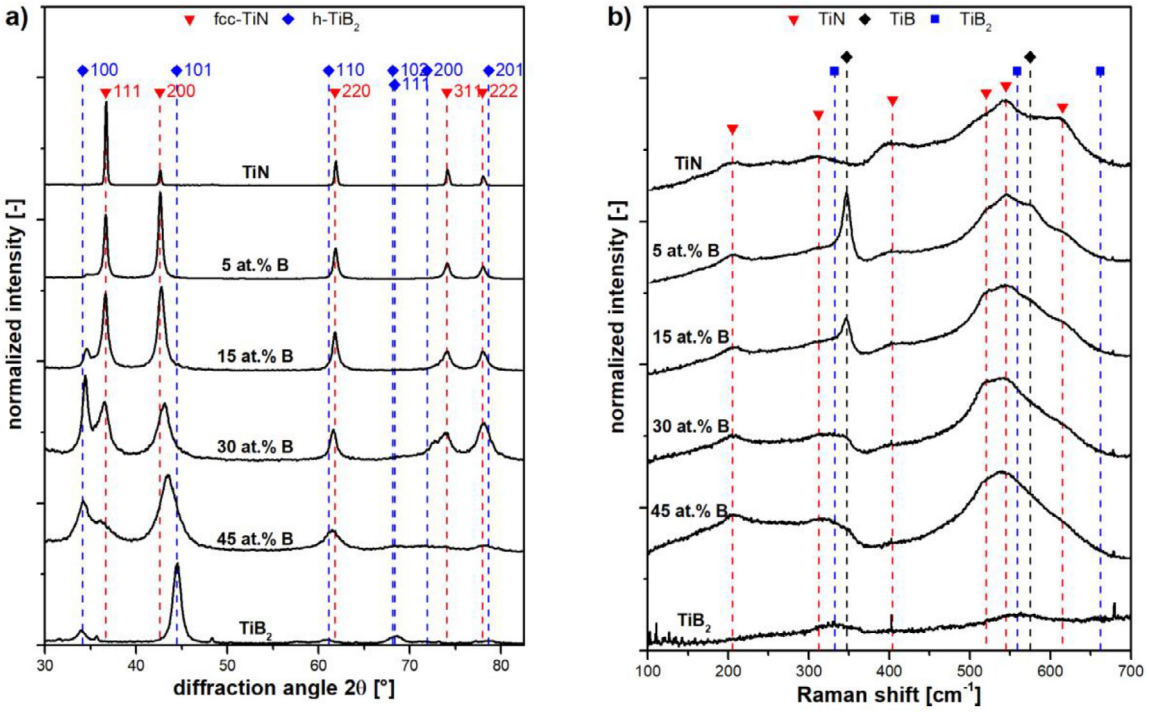

Fig. 2. (a) X-ray diffractograms and (b) Raman spectra of the investigated TiN, TiN/Ti(B,N) and TiN/TiB_2 coatings.

ciency. Thus, the scans shown in Fig. 2b are again normalized. A relative comparison of the individual spectra already allows to survey the change from TiN to TiB_2. For pure TiN and samples with low B contents the most pronounced signal is the one related to the TiN phase [4,19,20], which was already identified via XRD. This pronounced signal changes considerably towards TiB_2 [4] at higher B contents, which is also in good agreement with the XRD results. However, in addition, for the 5 and 15 at.% B samples, a distinct peak at a wavenumber of ~350 cm^{-1} can be identified, which is neither related to TiN nor to TiB_2. This peak can be assigned to TiB, indicating an additional amorphous constituent at low B contents, since no evidence for a crystalline TiB phase is found in XRD [4].

Additional X-ray photoelectron spectroscopy (XPS) measurements, shown in Fig. 3, were performed to support the findings of the XRD and Raman measurements and in particular to confirm the presence of the presumably a-TiB phase. Within the Ti 2p orbital, peaks for Ti-N bonds can be seen in the spectrum for pure TiN [4,21], which continuously shift towards the bonding energy of Ti-B_2 [4,21] with increasing B content. This agrees well with the N 1 s spectra, showing a typical Ti-N peak [4,21] that decreases in intensity with increasing B content and completely diminishes for TiB_2. Consistently, the B 1 s spectrum for TiN reveals a flat line. In accordance to the Raman measurements, a small peak for Ti-B [22,23] can be seen in the spectra of the 5 and 15 at.% B sample, but also the 30 at.% B sample still seems to exhibit a small Ti-B shoulder. While no distinct Ti-B_2 peak can be identified for the 5 at.% B sample, the samples with higher B contents unambiguously show Ti-B_2 peaks which increase in intensity with increasing B content.

In order to further investigate the spatial distribution of N and B and possible cluster formation within the Ti(B,N) coatings, APT measurements were performed which are presented in Fig. 4. At a first glance, the distribution of B atoms within the reconstructed tips was examined and checked for site specific B accumulations. The reconstruction of the sample with the lowest global B content of 5 at.%, shown in Fig. 4a, reveals obvious segregation of B atoms in a distinct plane-like manner, which appears to correlate with the grain boundaries of the sample. To obtain information on the elemental profile across a supposed grain boundary, a respective boundary was tagged via an isosurface (15 at.%

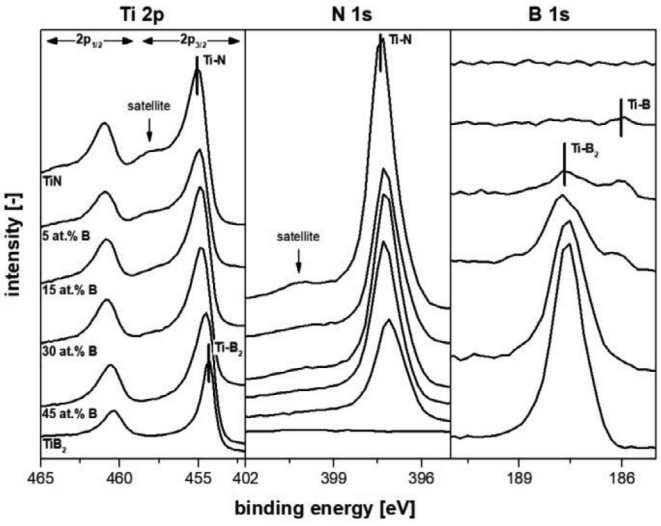

Fig. 3. Ti 2p, N 1 s and B 1 s XPS spectra of the investigated TiN, TiN/Ti(B,N) and TiN/TiB_2 coatings.

B) and a cylinder of Ø 10 nm and 25 nm in length was placed to intercept the assumed grain boundary. Its rotational symmetric axis was aligned normal to the interface and the elemental composition along the respective direction was analyzed. The corresponding elemental profile clearly shows an enrichment of B at the boundary, accompanied by N depletion and Ti decrease. For the chosen region, the elemental profile almost reaches the elemental ratio of a $Ti(B,N)_2$ compound which can be related to the faint h-TiB_2 peaks which were detected using XRD. Yet, a statistical evaluation of the B accumulations of the whole volume of this particular sample, using isosurfaces and proximity histograms (proxigrams), as performed later on for the samples with higher B contents, lead to high scatter in the obtained proxigrams and did not yield conclusive results. Thus, the B accumulations at the grain boundaries of

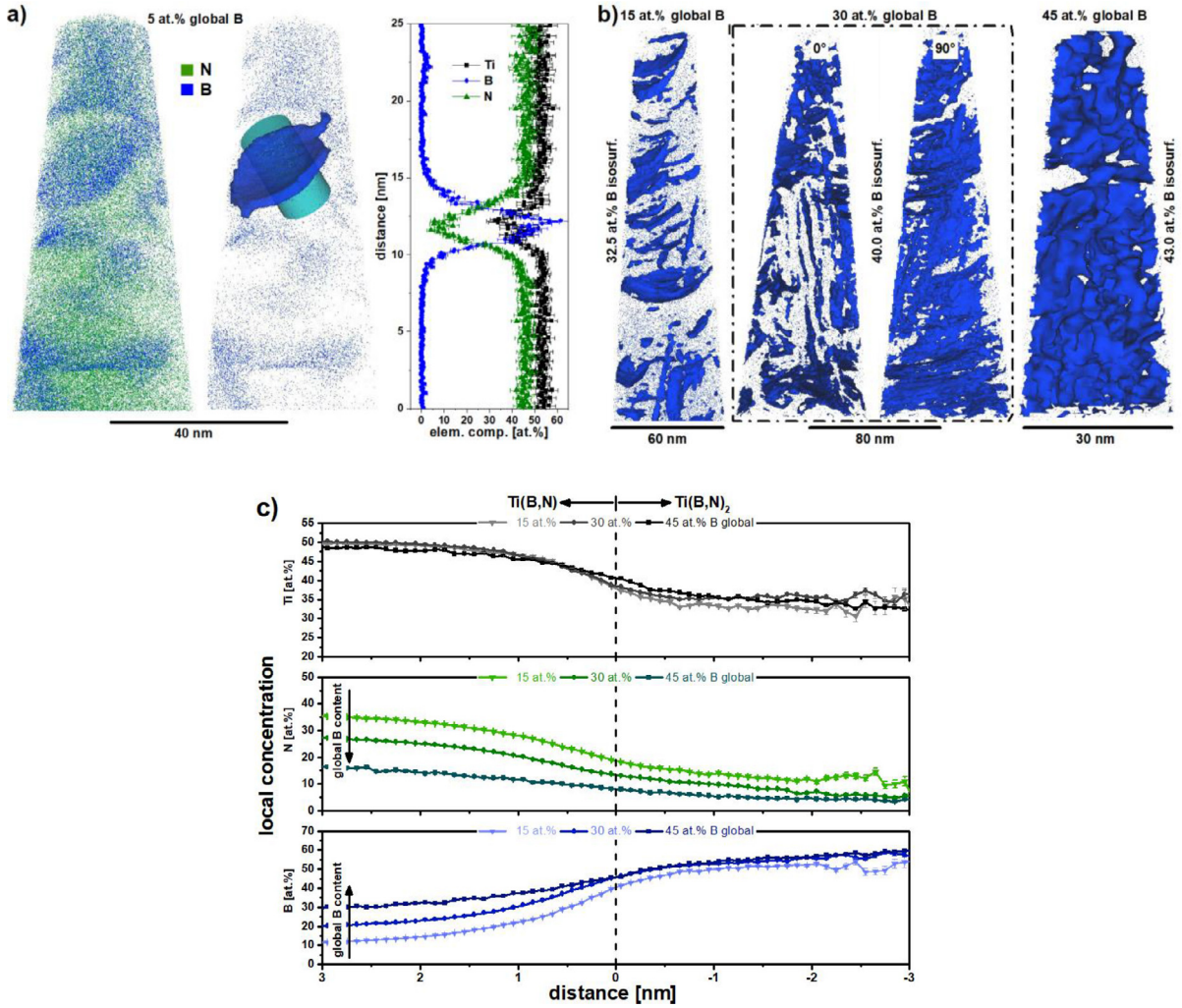

Fig. 4. (a) 3D APT reconstruction of 5 at.% B sample and corresponding elemental profile along the drawn cylinder through an assumed grain boundary. (b) 3D APT reconstructions including B isoconcentration surfaces and (c) their corresponding proximity histograms of the 15, 30 and 45 at.% B samples.

the 5 at.% B sample are considered as a mixture of h-Ti(B,N)$_2$, which was evidenced via XRD, and a-TiB, which is supported by the Raman and XPS measurements. No indication of larger B enriched Ti(B,N)$_2$ like clusters can be found within the reconstruction of the 5 at.% B sample. Within the reconstructions of the samples with higher global B contents, however, larger B enriched clusters are found. To visualize and further analyze these B enriched clusters, B isoconcentration surfaces with B concentrations adopted to the global B content of the individual samples, following the procedure suggested by Barton et al. [24] were created and subsequently analyzed using proximity histograms. The reconstructions, using corresponding isoconcentration values of 32.5, 40.0 and 43.0 at.% B for the tips with a global B content of 15, 30 (0 and 90° rotated) and 45 at.%, respectively, are presented in Fig. 4b. The reconstructions of the 15 and 30 at.% B samples again reveal accumulations in plane-like manner, similar to the 5 at.% B sample. This indicates that also for the samples with higher global B content, B-rich compounds are formed at the grain boundaries. The 15 at.% B sample and especially the 30 at.% B sample exhibit almost vertically aligned platelets, which are clearly visible when the 0° and 90° rotated reconstructions of the 30 at.% B sample are compared. Those platelets are related to the needle-like structure, evidenced within the SEM images in Fig. 1. For the 45 at.% B sample however, such features are not observed and the B accumulations seem to be statistically distributed throughout the whole volume of the reconstruction. The proximity histograms for Ti, N and B of the corresponding isosurfaces of the three coatings are presented in Fig. 4c. The Ti profiles, ranging from the outside towards the inside of the clusters corroborate the formation of Ti(B,N) and Ti(B,N)$_2$ based compounds with Ti fractions of ~1:1 and ~1:2. In addition, the B and N profiles do not reveal a discrete separation of B and N to pure nitride and boride phases. They show intermixing, which strongly correlates with the global B content, thus suggesting the formation of Ti(B,N) and Ti(B,N)$_2$ solid solutions rather than separation of pure TiN and TiB$_2$. The results indicate that the B content in both phases rises with increasing global B content and consequently, the N content shows the inverse trend. This observation however, seems to be more pronounced for the Ti(B,N) phase, while the degree of intermixing within Ti(B,N)$_2$ appears to be limited. Besides the strong separation into fcc and h-phase fractions as indicated by XRD, the measurements suggest that both phases, fcc-TiN and h-TiB$_2$, exhibit a pronounced solubility for the respective foreign element.

3.2. Mechanical properties

In addition to the observed microstructural changes, B addition considerably affects the mechanical properties of the investigated coatings as can be seen for the hardness and Young´s modulus in Fig. 5. While the Young´s modulus of all samples, with exception of the 45 at.% B sample (337 ± 7 GPa), lies within a close range of ~480-540 ± 20 GPa, the hardness of 18.3 ± 0.8 GPa of the TiN sample is already significantly increased to 28.4 ± 0.4 GPa for the addition of 5 at.% B. Further increasing

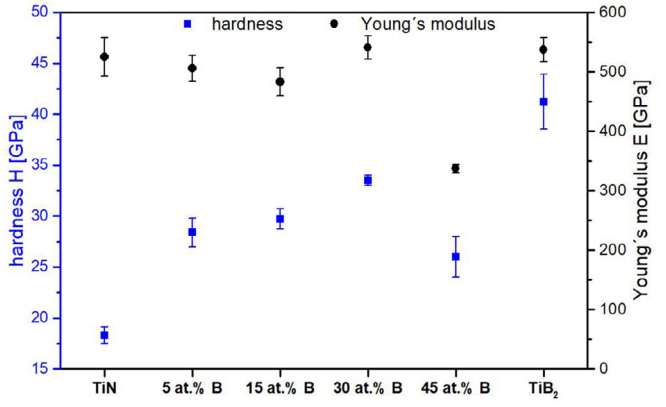

Fig. 5. Hardness and Young´s modulus of the investigated TiN, TiN/Ti(B,N) and TiN/TiB_2 coatings obtained via nanoindentation experiments.

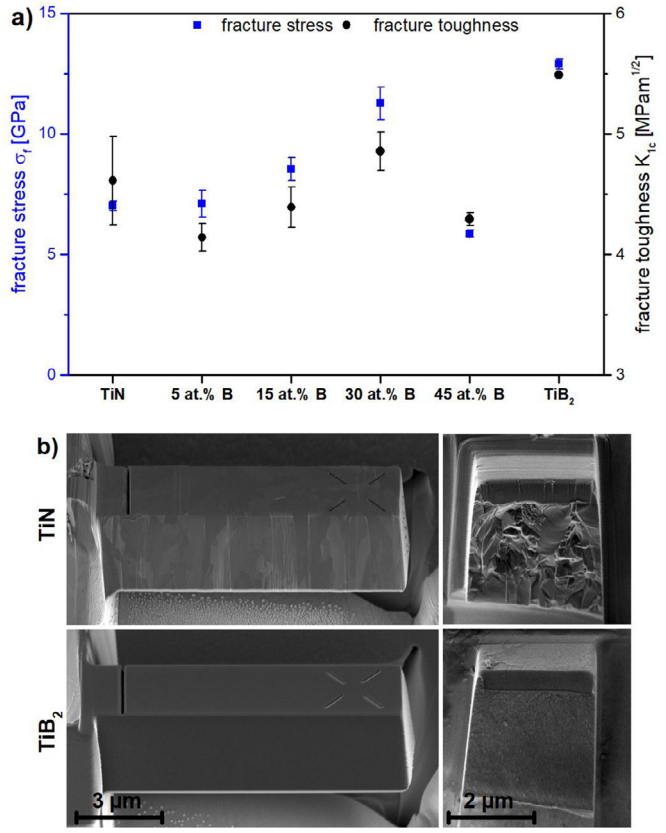

Fig. 6. (a) Fracture stress and toughness of the investigated TiN, TiN/Ti(B,N) and TiN/TiB_2 coatings obtained via micromechanical bending experiments and (b) exemplary microcantilevers of TiN and TiB_2 before and after fracture.

the B content results in a further rise in hardness to 29.7 ± 1.0 GPa and 33.5 ± 0.5 GPa for 15 and 30 at.% B, respectively, and 41.2 ± 2.7 GPa for pure TiB_2. Again, the only exception is the sample with 45 at.% B, having a comparatively low hardness of 26.0 ± 2.0 GPa.

For a thorough understanding of the mechanical properties of the investigated coatings, their fracture behavior was investigated via micromechanical bending tests, revealing their fracture stress and fracture toughness which are shown in Fig. 6a. In contrast to the abrupt rise in hardness, first addition of B does not change the fracture stress significantly (7.0 ± 0.2 GPa for TiN vs. 7.1 ± 0.5 GPa for 5 at.% B). The fracture toughness is even slightly reduced from 4.6 ± 0.4 $MPam^{1/2}$ for TiN to 4.1 ± 0.1 $MPam^{1/2}$ for Ti(B,N) with 5 at.% B. With further increasing B content however, a steadily increasing fracture stress and toughness up to values of 11.3 ± 0.7 GPa and 4.9 ± 0.2 $MPam^{1/2}$, respectively, at a B content of 30 at.% are observed. With a fracture stress of 5.9 ± 0.2 GPa and a fracture toughness of 4.3 ± 0.1 $MPam^{1/2}$, the 45 at.% B sample again represents an exception, exhibiting the lowest fracture stress and second lowest fracture toughness of all investigated samples. Similar to the hardness, TiB_2 also exhibits the highest fracture stress and toughness of 12.9 ± 0.2 GPa and 5.5 ± 0.1 $MPam^{1/2}$, respectively. Exemplary, notched microcantilevers and their corresponding fracture surfaces which were used for the determination of the fracture toughness are shown in Fig. 6b for TiN and TiB_2. The coarse-grained microstructure of TiN can be clearly identified via the bright and dark contrast throughout the cantilever, representing differently oriented individual grains. In contrast to that, the TiB_2 cantilever appears rather homogenous without any pronounced change in contrast within the cantilever, which is representative for the microstructure of the TiB_2 sample with grains in the nm range. In accordance with that, also the fracture surfaces exhibit a quite different appearance. While for the TiN cantilever the fracture surface exhibits a rather pronounced topography, suggesting a mixed trans- and intergranular fracture behavior, the fracture surface of the TiB_2 cantilever appears quite smooth and featureless and at that scale does not yield any conclusion about the specific fracture behavior.

4. Discussion

For the coatings investigated within this work, a strong influence of the $BCl_3/TiCl_4$ ratio (i.e. the B content) on the deposition rate is observed, which significantly increases with increasing B content, similarly to observations in the work of Holzschuh [2]. In addition, the surface topography is considerably affected by the B content, which is also in accordance with previous reports e.g. by Holzschuh [2] or Wagner et al. [3]. Cross-sectional SEM images shown in this work indicate a similar microstructure as observed for a graded Ti(B,N) coating investigated within one of our previous works [6]. The observed needle-like structure, which is visible within the cross-sections and on the coating surfaces, seems to be a characteristic feature of Ti(B,N) coatings with moderate B content [3,7,8]. Also the evolution of grain size and shape of the herein investigated individual TiN/Ti(B,N) bi-layer coatings is in good agreement with transmission electron microscopy (TEM) investigations performed on a graded Ti(B,N) coating shown in our previous work [6]. The decreasing grain size with increasing B content is further corroborated by the XRD measurements, which reveal a decreasing domain size, which can be used as an estimate of the grain size [25]. The determined domain size for TiB_2 agrees well with values reported by Schalk et al. [5] for a similar TiB_2 coating investigated by synchrotron X-ray nanodiffraction. In contrast, the TiN single-layer coating investigated within this work exhibits a much larger domain size than the one determined by Schalk et al. [5] for the significantly thinner TiN baselayer of the investigated TiN/TiB_2 bilayer coating. This can be related to the distinct difference in coating thickness, resulting in much larger domains for the TiN coating investigated within this work as a result of pronounced competitive growth. In accordance with reports by Dreiling et al. [4] and Kainz et al. [7], faint peaks of h-TiB_2 were already found for the sample containing 5 at.% B by XRD and for samples with B contents ≤ 30 at.% B and Raman spectroscopy and XPS consistently indicated the formation of TiB. Analogously to those earlier works, also for the present work it can be concluded that the identified TiB phase is amorphous, since no evidence for crystalline TiB could be detected using XRD. In addition, the APT measurement of the 5 at.% B sample performed within this work indicates that the B within this sample accumulates in a distinct plane-like manner, which can be attributed to accumulation at the grain boundaries of the Ti(B,N), confirming observations of previous works [7].

For higher B contents, a fcc/h dual-phase structure is observed via XRD, while the additional a-TiB phase diminishes, as corroborated by Raman spectroscopy and XPS. Thus, further attention should be paid to

the elemental composition of the fcc- and h-phase fractions. The ERDA measurements performed within this work are not conclusive with respect to the phase composition and do not provide further information on the degree of intermixing of B and N. The XRD measurements indicate the formation of mixtures of fcc-TiN and h-TiB_2 for all investigated Ti(B,N) coatings, which would be in accordance with the works of Dreiling et al. and Holzschuh [2,4]. This however, is in contrast to the herein presented APT results, which clearly reveal pronounced intermixing and thus indicate the formation of fcc-Ti(B,N) and h-$Ti(B,N)_2$. Yet, this is not clearly reflected in the lattice parameters of the respective phases obtained via XRD which consequently should follow a Vegard´s like behavior. For the h-phase no adequate reference for h-TiN_2 could be found, thus no prediction for the lattice parameters of the h-$Ti(B,N)_2$ phase can be provided. For the fcc-phase, however, the well-established fcc-TiN with a lattice parameter of 4.242 Å (PDF 00–038–1420 [18]) can be found, and also a fcc-TiB phase with a reported lattice parameter of 4.202 Å (PDF 01–089–3922 [18]) is available within the ICDD database. These tabulated values suggest a trend towards a smaller lattice parameter with increasing B content of the fcc-Ti(B,N) phase. However, this expected trend is not confirmed by the lattice parameters determined from the performed XRD measurements. A closer look at the reference PDF of fcc-TiB yields a possible explanation, since uncertainties concerning the unit cell data are mentioned within the comments section of that PDF. The original reference by Ehrlich [26] claiming a fcc-TiB phase with a lattice parameter of 4.202 Å in 1949 was already contested by Brewer et al. [27] in 1951, and thus, seems rather unreliable. In contrast to that, ab initio calculations provided by Mayrhofer et al. [28,29] suggested a much higher value of 4.535 Å for fcc-TiB, which is not experimentally validated though. Considering the APT measurements and the obtained metal to non-metal ratios of the identified Ti(B,N) and $Ti(B,N)_2$ compounds, also a substitution of B within the metal sub-lattice and consequent influence on the lattice parameter, as suggested by Mayrhofer et al. in another work [30], can be excluded for the coatings investigated within this work. Finally, a recent experimental work by Hu et al. [31], investigating the formation of pure fcc-TiB nanoparticles by boronizing Ti powders, may explain the constant lattice parameters within a large compositional range. They reported a lattice parameter of ~4.245 Å for their fcc-TiB nanoparticles, which is similar to the lattice parameter of fcc-TiN. This might be the reason why, despite the obvious formation of a fcc-Ti(B,N) solid solution, no clear trend in the lattice parameter of the fcc-phase could be deduced within this work. For the h-$Ti(B,N)_2$, a plausible prediction of lattice parameters cannot be provided due to a lack of available reference values for the hypothetical h-TiN_2 phase. Yet it can be summarized that the present phase composition of the investigated coatings consists of fcc-Ti(B,N), h-$Ti(B,N)_2$ and additional fractions of a-TiB, which accumulates at the grain boundaries at lower global B contents.

To further elucidate the microstructural evolution, ab initio calculations for the respective structures were performed (calculation details and additional information can be found in the supplemental material). Initial structural models of fcc-Ti(B,N) and h-$Ti(B,N)_2$ were fully relaxed and the resulting energies of formation, E_f, are shown in Fig. 7. The fcc-Ti(B,N) structures clearly maintained their fcc rock salt (B1) crystal structure even after the full relaxation; E_f increases with increasing B content and exhibits a slight downwards bowing corresponding to negative mixing enthalpy. Therefore, fcc-Ti(B,N) is predicted stable with respect to decomposition into fcc-TiN and hypothetical fcc-TiB. Noteworthy, a-TiB yields lower E_f than the fcc-TiB, thus being predicted more stable. Contrarily, the h-$Ti(B,N)_2$ supercells maintain their hexagonal structure only up to N content of ~24 at.% on the non-metal sublattice of h-$Ti(B,N)_2$. For higher N content, the supercells undergo significant structural relaxations leading to an apparent amorphization (see inset in Fig. 7 for a N content of ~74 at.%). A hypothetical TiN_2 could be stabilized due to symmetries and the relaxation taking place at 0 K, however, the corresponding $E_f > 0$ suggests chemical instability of this compound. From this behavior it can be concluded that B in fcc-Ti(B,N) is less detrimental for the structure than N in the h-$Ti(B,N)_2$, and hence higher solubility of B in fcc-TiN can be expected than N in h-TiB_2. Finally, all these structures are unstable with respect to decomposition to pure fcc-TiN and h-TiB_2.

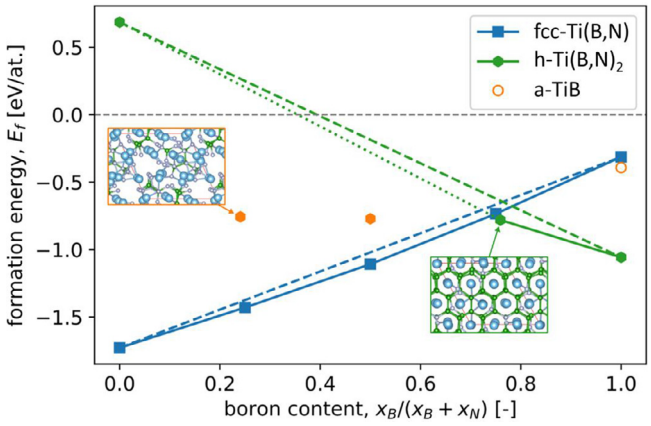

Fig. 7. Energy of formation of fcc-Ti(B,N) and h-$Ti(B,N)_2$ systems as functions of the B content of the non-metal atoms. The orange circle corresponds to a-TiB, while the open orange hexagons denote h-$Ti(B,N)_2$ structures with strong structural relaxations (amorphized structures).

Those conclusions are fully in line with the experimental observations. Firstly, all coatings containing B and N at the same time were experimentally shown to be two-phase systems composed of fcc-Ti(B,N) and h-$Ti(B,N)_2$, the 5 at.% B coating being the only exception with fcc-TiN grains seemingly separated by a mixture of h-$Ti(B,N)_2$ and a-TiB tissue phase. Secondly, the APT proxigrams in Fig. 4 clearly suggest that the composition of h-$Ti(B,N)_2$ varies only marginally with the overall B content, unlike that of the fcc-Ti(B,N) phase. This agrees with B being less hostile to the fcc-TiN phase than N to the h-TiB_2 phase, based on the structural analysis. Thirdly, inspecting the proxigrams of the different samples closer, it seems that the B and N content within the observed fcc-Ti(B,N) and h-$Ti(B,N)_2$ phases do not exactly reach a plateau, but still exhibit a slight gradient with increasing distance from the isosurfaces. This indicates that the equilibrium composition of the respective compounds might not yet be reached, which is in line with the predicted energies of formation suggesting that eventually the binary fcc-TiN and h-TiB_2 are the most stable configuration in the quasi-binary TiN-TiB_2 system.

With regard to the mechanical properties of the investigated coatings, similar to previous works [2,6,7], a very pronounced effect of already rather low B contents on the hardness is observed. This initial hardness increase is commonly attributed to the observed decrease in grain size with B addition, in the present case causing the hardness of ~18 GPa of TiN to instantly increase to ~28 GPa for the coating with 5 at.% B, representing a hardness gain of ~55%. Since only minor fractions of the h-$Ti(B,N)_2$ hard phase were indicated by XRD for this sample, the significant increase in hardness seems to be mainly related to the grain size and possible contributions of solid solution hardening of the fcc-Ti(B,N) phase [32]. With further increasing B content, at moderate compositions, still an increasing hardness is observed but the effect is less pronounced. This might be interpreted as result of the increasing fraction of h-$Ti(B,N)_2$ hard phase, and thus a shift towards a more covalently bonded material, while the effect of the decreasing crystallite size might be already fully exploited at low B contents. The sample with a global B content of 45 at.% states an exception with a comparatively low hardness of ~26 GPa, which in our previous work [6] could be attributed to i) its porous structure and ii) a predominantly single-phase, but yet not ideal h-$Ti(B,N)_2$ structure, which obviously deteriorate the mechanical properties of the coating. For clarity, two TEM images of the 45 at.% B layer of a graded Ti(B,N) coating investigated within our

previous work [6] confirming the porosity for this B-content are provided within the supplemental material. The pure h-TiB_2, however, exhibited the highest hardness of ~41 GPa of all investigated coatings, in agreement with previously reported values [5,6], which can be related to the strong covalent bonding character of TiB_2 [28]. In contrast to the pronounced change in hardness of the investigated samples, the Young´s modulus of all but the 45 at.% B sample, stayed within a range of ~475–550 GPa (with TiN and TiB_2 yielding 525 ± 32 GPa and 537 ± 20 GPa, respectively) and did not reveal any indicative trend. This is in accordance with reported values for TiN [33,34] and TiB_2 [35,36], both lying within a range of ~440–590 GPa, thus not suggesting a significant change with changing phase composition.

Considering the fracture stress of the investigated coatings, the obtained value of 7.0 ± 0.2 GPa for TiN is significantly higher than the value of 3.9 ± 0.5 GPa previously reported by Kainz et al. [7,8] for a comparable CVD TiN coating. That is most likely owed to improved process parameters for TiN deposition since thermally activated CVD usually operates close to thermal equilibrium. Thus, if the process parameters are well-chosen, a rather high-quality microstructure with well-defined crystals and few defects can be produced, resulting in improved fracture properties. But it may also partly be related to a difference in preferred orientation. While the CVD TiN investigated by Kainz et al. was essentially free of any preferred orientation, the TiN coating investigated within this work, appears to rather show a 111 texture, considering the X-ray diffractogram shown in Fig. 2a, which might additionally influence its fracture stress. This assumption is supported by a recent work of Buchinger et al. [37], reporting on significant differences of theoretically predicted TiN (111), (110) and (100) surface energies. The change in fracture stress with initial B addition observed within this work is marginal and the determined value of 7.1 ± 0.5 GPa for the 5 at.% B sample is comparable to the CVD Ti(B,N) coatings investigated by Kainz et al. [7,8]. The rather small change, which is a bit in contradiction to the significant change in grain size, can be explained by the probable change (i.e. loss) of the preferred orientation. In contrast to the TiN coating, the Ti(B,N) coating with 5 at.% B investigated within this work is essentially free of any texture. Further, the chemical bonding, an important factor affecting the fracture behavior of a material, is merely changed at such low B contents. With further B addition, however, a significantly increasing fracture stress (with exception of the 45 at.% B sample) is observed, which is most likely related to the increasing fraction of strong covalent bonds due to the h-$Ti(B,N)_2$ phase. The highest fracture stress of all investigated coatings was found with 12.9 ± 0.2 GPa for the pure TiB_2 coating which is in good agreement with a recent work by Gruber et al. [38], reporting 12.1 ± 1.0 GPa for a similar CVD TiB_2 coating.

Similar to the fracture stress, the TiN coating exhibits with 4.6 ± 0.4 $MPam^{1/2}$ a higher fracture toughness than CVD TiN previously investigated by Kainz et al. [7,8], who reported values of ~2.5 $MPam^{1/2}$. Also compared to recently reported values of ~2–3 $MPam^{1/2}$ for physically vapor deposited (PVD) TiN [37,39], the fracture toughness determined within this work is significantly higher. Yet, the herein reported value seems to line up quite well with values for sintered bulk TiN, ranging from 4.1 to 5.6 $MPam^{1/2}$ [40–42]. This seems reasonable considering the rather high-quality microstructure of well-developed CVD processes with well-defined crystals and few defects. For the B containing coatings investigated within this work, however, initial addition of 5 at.% B seems to deteriorate the toughness. This might, on the one hand, be a result of the loss of a probable preferred orientation which is, as stated above, assumed to beneficially influence the toughness of the pure TiN. On the other hand, it might be owed to the presence and segregation of initial fractions of h-$Ti(B,N)_2$ and the amorphous TiB phase at the grain boundaries. With further increasing B content, to values > 5 at.% B, the toughness rises (again with exception of the 45 at.% sample), which similarly to the increase in fracture stress is assumed to be a result of the change of chemical bonding within the investigated samples. For the pure TiB_2, again the determined value of 5.5 ± 0.1 $MPam^{1/2}$ is in good agreement with the fracture toughness values of its corresponding sintered counterparts [36,43], while again comparable PVD representatives are considerably lower [44]. In addition to the quantitative differences, a significant difference in appearance of the fracture surfaces of the different coatings investigated within this work is observed, as shown in Fig. 6b for pure TiN and TiB_2. This is attributed to the significant change in microstructure as previously reported by Kainz et al. [7,8]. However, generally it should be noted that while the toughness from TiN towards TiB_2 is increased by almost 20%, realistically interpreted, the investigated coatings still have to be considered as rather brittle, which is also reflected in their purely linear elastic fracture behavior until instantaneous fatal fracture.

5. Conclusions

The samples investigated within this work clearly reveal the feasibility for the industrial deposition of Ti(B,N) coatings with a B content freely adjustable between pure TiN and TiB_2. A face-centered cubic (fcc)/hexagonal (h) mixed structure with minor fractions of amorphous (a) TiB at low B contents was found. Accumulation of this a-TiB phase at the grain boundaries was indicated via atom probe tomography (APT). With increasing B content, the h-phase fraction steadily increased and for the sample with 45 at.% B an apparently almost single-phase h-structure was predominant. For all Ti(B,N) samples, APT revealed the formation of fcc-Ti(B,N) and h-$Ti(B,N)_2$ solid solutions. These observations were corroborated by ab initio calculations, thereby increasing the plausibility of the determined microstructural complexity. A higher degree of intermixing within fcc-Ti(B,N) as compared with h-$Ti(B,N)_2$ was predicted by the calculations and experimentally confirmed by APT. While the pure h-TiB_2 showed the highest hardness, fracture stress and fracture toughness of all investigated coatings, the Ti(B,N) coatings with a dual-phase fcc/h microstructure demonstrated a significant impact of the B content on their mechanical properties, with the sample having a B content of 30 at.% being the most promising one. In contrast to that, the sample with a B content of 45 at.% revealed deteriorated mechanical properties, which were related to its porosity and possibly to the predominantly h, but yet not ideal h-TiB_2 structure. Thus, it can be concluded that a significant gain in hardness, fracture stress and toughness of TiN coatings can be achieved by B addition as long as a dual-phase fcc/h microstructure can be maintained. However, the results also indicate that coatings with high B contents already having a predominant h-structure should be avoided. An additional advantage of fcc-dominated Ti(B,N) coatings over TiN/TiB_2 is the avoidance of the abrupt transition from fcc to h-structure from the fcc-TiN base-layer to the h-TiB_2 top-layer, which usually results in weak bonding and subsequently adhesion problems. Consequently, the fcc-dominated Ti(B,N) coatings with high B content investigated within this work represent a promising alternative to complement or even replace TiB_2 within the well-established TiN/TiB_2.

Declaration of competing interest

The authors declare that they have no known competing financial interests or personal relationships that could have appeared to influence the work reported in this paper.

Acknowledgements

The authors gratefully acknowledge the financial support under the scope of the COMET program within the K2 Center “Integrated Computational Material, Process and Product Engineering (IC-MPPE)” (Project No 859480). This program is supported by the Austrian Federal Ministries for Climate Action, Environment, Energy, Mobility, Innovation and Technology (BMK) and for Digital and Economic Affairs (BMDW), represented by the Austrian research funding association (FFG), and the federal states of Styria, Upper Austria and Tyrol. The financial support

by the Austrian Federal Ministry for Digital and Economic Affairs and the National Foundation for Research, Technology and Development is gratefully acknowledged. The computational results presented have been achieved [in part] using the Vienna Scientific Cluster (VSC).

Supplementary materials

Supplementary material associated with this article can be found, in the online version, at doi:10.1016/j.mtla.2022.101323.

References

[1] H. Holzschuh, Chemical-vapor deposition of wear resistant hard coatings in the Ti–B–C–N system: properties and metal-cutting tests, Int. J. Refract. Met. Hard Mater. 20 (2002) 143–149, doi:10.1016/S0263-4368(02)00013-6.
[2] H. Holzschuh, Deposition of Ti–B–N (single and multilayer) and Zr–B–N coatings by chemical vapor deposition techniques on cutting tools, Thin Solid Films 469–470 (2004) 92–98, doi:10.1016/j.tsf.2004.08.077.
[3] J. Wagner, D. Hochauer, C. Mitterer, M. Penoy, C. Michotte, W. Wallgram, M. Kathrein, The influence of boron content on the tribological performance of Ti–N–B coatings prepared by thermal CVD, Surf. Coat. Technol. 201 (2006) 4247–4252, doi:10.1016/j.surfcoat.2006.08.071.
[4] I. Dreiling, C. Raisch, J. Glaser, D. Stiens, T. Chassé, Characterization and oxidation behavior of MTCVD Ti–B–N coatings, Surf. Coat. Technol. 206 (2011) 479–486, doi:10.1016/j.surfcoat.2011.07.067.
[5] N. Schalk, J. Keckes, C. Czettl, M. Burghammer, M. Penoy, C. Michotte, C. Mitterer, Investigation of the origin of compressive residual stress in CVD TiB_2 hard coatings using synchrotron X-ray nanodiffraction, Surf. Coat. Technol. 258 (2014) 121–126, doi:10.1016/j.surfcoat.2014.09.050.
[6] M. Tkadletz, N. Schalk, C. Mitterer, J. Keckes, M. Pohler, C. Czettl, Cross-sectional characterization techniques as the basis for knowledge-based design of graded CVD TiN-TiB_2 coatings, Int. J. Refract. Met. Hard Mater. 71 (2018) 280–284, doi:10.1016/j.ijrmhm.2017.11.043.
[7] C. Kainz, N. Schalk, M. Tkadletz, C. Mitterer, C. Czettl, Microstructure and mechanical properties of CVD TiN/TiBN multilayer coatings, Surf. Coat. Technol. 370 (2019) 311–319, doi:10.1016/j.surfcoat.2019.04.086.
[8] C. Kainz, N. Schalk, M. Tkadletz, C. Mitterer, C. Czettl, The effect of B and C addition on microstructure and mechanical properties of TiN hard coatings grown by chemical vapor deposition, Thin Solid Films 688 (2019) 137283, doi:10.1016/j.tsf.2019.05.002.
[9] C. Kainz, N. Schalk, M. Tkadletz, C. Saringer, M. Winkler, A. Stark, N. Schell, J. Julin, C. Czettl, Thermo-physical properties of coatings in the Ti(B,N) system grown by chemical vapor deposition, Surf. Coat. Technol. 384 (2020) 125318, doi:10.1016/j.surfcoat.2019.125318.
[10] U. Schleinkofer, C. Czettl, C. Michotte, Coating Applications for Cutting Tools, Elsevier Ltd, 2014, doi:10.1016/B978-0-08-096527-7.00016-7.
[11] P.H. Mayrhofer, R. Rachbauer, D. Holec, F. Rovere, J.M. Schneider, Protective Transition Metal Nitride Coatings, Elsevier, 2014, doi:10.1016/B978-0-08-096532-1.00423-4.
[12] R. Kullmer, C. Lugmair, A. Figueras, J. Bassas, M. Stoiber, C. Mitterer, Microstructure, mechanical and tribological properties of PACVD Ti(B,N) and TiB_2 coatings, Surf. Coat. Technol. 174–175 (2003) 1229–1233, doi:10.1016/S0257-8972(03)00532-2.
[13] C. Czettl, J. Thurner, U. Schleinkofer, Knowledge based coating design of CVD TiN-TiBN-TiB_2 architecture, Int. J. Refract. Met. Hard Mater. 71 (2018) 330–334, doi:10.1016/j.ijrmhm.2017.11.040.
[14] K. Thompson, D. Lawrence, D.J. Larson, J.D. Olson, T.F. Kelly, B. Gorman, In situ site-specific specimen preparation for atom probe tomography, Ultramicroscopy 107 (2007) 131–139, doi:10.1016/j.ultramic.2006.06.008.
[15] L.J.S. Johnson, M. Thuvander, K. Stiller, M. Odén, L. Hultman, Spinodal decomposition of $Ti_{0.33}Al_{0.67}N$ thin films studied by atom probe tomography, Thin Solid Films 520 (2012) 4362–4368, doi:10.1016/j.tsf.2012.02.085.
[16] W.C. Oliver, G.M. Pharr, An improved technique for determining hardness and elastic modulus using load and displacement sensing indentation experiments, J. Mater. Res. 7 (1992) 1564–1583, doi:10.1557/JMR.1992.1564.
[17] K. Matoy, H. Schönherr, T. Detzel, T. Schöberl, R. Pippan, C. Motz, G. Dehm, A comparative micro-cantilever study of the mechanical behavior of silicon based passivation films, Thin Solid Films 518 (2009) 247–256, doi:10.1016/j.tsf.2009.07.143.
[18] S. Gates-Rector, T. Blanton, The powder diffraction file: a quality materials characterization database, Powder Diffr 34 (2019) 352–360, doi:10.1017/S0885715619000812.
[19] M. Stoehr, C.S. Shin, I. Petrov, J.E. Greene, Raman scattering from TiN_x ($0.67 \leq x \leq 1.00$) single crystals grown on MgO(001), J. Appl. Phys. 110 (2011) 083503, doi:10.1063/1.3651381.
[20] C.P. Constable, J. Yarwood, W.D. Münz, Raman microscopic studies of PVD hard coatings, Surf. Coat. Technol. 116–119 (1999) 155–159, doi:10.1016/S0257-8972(99)00072-9.
[21] R. Ali, E. Alkhateeb, F. Kellner, S. Virtanen, N. Popovska-Leipertz, Chemical vapor deposition of titanium based ceramic coatings on low carbon steel: characterization and electrochemical evaluation, Surf. Coat. Technol. 205 (2011) 5454–5463, doi:10.1016/j.surfcoat.2011.06.014.
[22] Y.H. Lu, Y.G. Shen, Z.F. Zhou, K.Y. Li, Effects of nitrogen content on microstructure and oxidation behaviors of Ti–B–N nanocomposite thin films, J. Vac. Sci. Technol. A Vacuum, Surfaces, Film 24 (2006) 340–349, doi:10.1116/1.2172949.
[23] C.M.T. Sanchez, H.D. Fonseca-Filho, M.E.H. Maia da Costa, F.L. Freire, Nitrogen incorporation into titanium diboride films deposited by dc magnetron sputtering: structural modifications, Thin Solid Films 517 (2009) 5683–5688, doi:10.1016/j.tsf.2009.02.122.
[24] D.J. Barton, B.C. Hornbuckle, K.A. Darling, G.B. Thompson, The influence of Isoconcentration surface selection in quantitative outputs from proximity histograms, Microsc. Microanal. 25 (2019) 401–409, doi:10.1017/S143192761900014X.
[25] A. Fajar, E.Kartini Gunawan, H. Mugirahardjo, M. Ihsan, Crystallite size and microstrain measurement of cathode material after mechanical milling using neutron diffraction technique, Atom Indonesia 36 (2010) 111–115, doi:10.17146/aij.2010.27.
[26] P. Ehrlich, Über die binären Systeme des Titans mit den Elementen Stickstoff, Kohlenstoff, Bor und Beryllium, Zeitschrift für Anorg. Chemie. 259 (1949) 1–41, doi:10.1002/zaac.19492590102.
[27] L. Brewer, D.L. Sawyer, D.H. Templeton, C.H. Dauben, A study of the refractory borides, J. Am. Ceram. Soc. 34 (1951) 173–179, doi:10.1111/j.1151-2916.1951.tb11631.x.
[28] P.H. Mayrhofer, C. Mitterer, H. Clemens, Self-organized nanostructures in hard ceramic coatings, Adv. Eng. Mater. 7 (2005) 1071–1082, doi:10.1002/adem.200500154.
[29] P.H. Mayrhofer, M. Stoiber, C. Mitterer, Age hardening of PACVD TiBN thin films, Scr. Mater. 53 (2005) 241–245, doi:10.1016/j.scriptamat.2005.03.031.
[30] P.H. Mayrhofer, M. Stoiber, Thermal stability of superhard Ti–B–N coatings, Surf. Coat. Technol. 201 (2007) 6148–6153, doi:10.1016/j.surfcoat.2006.08.132.
[31] J. Hu, X. Dong, S. Tosto, Microstructure of face centered Cubic (fcc) TiB powder Synthesized by Boronizing of Ti powder, J. Am. Ceram. Soc. 95 (2012) 2089–2092, doi:10.1111/j.1551-2916.2012.05229.x.
[32] W. Soboyejo, Mechanical Properties of Engineered Materials, CRC Press, New York, 2002, doi:10.1201/9780203910399.
[33] G. Abadias, Stress and preferred orientation in nitride-based PVD coatings, Surf. Coat. Technol. 202 (2008) 2223–2235, doi:10.1016/j.surfcoat.2007.08.029.
[34] Y. Yang, H. Lu, C. Yu, J.M. Chen, First-principles calculations of mechanical properties of TiC and TiN, J. Alloys Compd. 485 (2009) 542–547, doi:10.1016/j.jallcom.2009.06.023.
[35] H. Ledbetter, T. Tanaka, Elastic-Stiffness Coefficients of Titanium Diboride, J. Res. Natl. Inst. Stand. Technol. 114 (2009) 333, doi:10.6028/jres.114.024.
[36] R.G. Munro, Material properties of titanium diboride, J. Res. Natl. Inst. Stand. Technol. 105 (2000) 709, doi:10.6028/jres.105.057.
[37] J. Buchinger, L. Löfler, J. Ast, A. Wagner, Z. Chen, J. Michler, Z.L. Zhang, P.H. Mayrhofer, D. Holec, M. Bartosik, Fracture properties of thin film TiN at elevated temperatures, Mater. Des. 194 (2020) 108885, doi:10.1016/j.matdes.2020.108885.
[38] D.P. Gruber, J. Zalesak, J. Todt, M. Tkadletz, B. Sartory, J.-P. Suuronen, T. Ziegelwanger, C. Czettl, C. Mitterer, J. Keckes, Surface oxidation of nanocrystalline CVD TiB_2 hard coatings revealed by cross-sectional nano-analytics and in-situ micro-cantilever testing, Surf. Coat. Technol. 399 (2020) 126181, doi:10.1016/j.surfcoat.2020.126181.
[39] M. Bartosik, C. Rumeau, R. Hahn, Z.L. Zhang, P.H. Mayrhofer, Fracture toughness and structural evolution in the TiAlN system upon annealing, Sci. Rep. 7 (2017) 16476, doi:10.1038/s41598-017-16751-1.
[40] H. Kuwahara, N. Mazaki, M. Takahashi, T. Watanabe, X. Yang, T. Aizawa, Mechanical properties of bulk sintered titanium nitride ceramics, Mater. Sci. Eng. A. 319–321 (2001) 687–691, doi:10.1016/S0921-5093(01)00936-4.
[41] B.M. Moshtaghioun, D. Gómez-García, A. Domínguez-Rodríguez, Spark plasma sintering of titanium nitride in nitrogen: does it affect the sinterability and the mechanical properties? J. Eur. Ceram. Soc. 38 (2018) 1190–1196, doi:10.1016/j.jeurceramsoc.2017.12.029.
[42] H. Borodianska, T. Ludvinskaya, Y. Sakka, I. Uvarova, O. Vasylkiv, Bulk $Ti_{1-x}Al_xN$ nanocomposite via spark plasma sintering of nanostructured $Ti_{1-x}Al_xN$–AlN powders, Scr. Mater. 61 (2009) 1020–1023, doi:10.1016/j.scriptamat.2009.08.019.
[43] S.D. Conzone, W.R. Blumenthal, J.R. Vainer, Fracture Toughness of TiB_2 and B_4C Using the Single-Edge Precracked beam, indentation strength, chevron notched beam, and indentation strength methods, J. Am. Ceram. Soc. 78 (1995) 2187–2192, doi:10.1111/j.1151-2916.1995.tb08634.x.
[44] J. Thörnberg, J. Palisaitis, N. Hellgren, F.F. Klimashin, N. Ghafoor, I. Zhirkov, C. Azina, J.-L. Battaglia, A. Kusiak, M.A. Sortica, J.E. Greene, L. Hultman, I. Petrov, P.O.Å. Persson, J. Rosen, Microstructure and materials properties of understoichiometric TiB_x thin films grown by HiPIMS, Surf. Coat. Technol. 404 (2020) 126537, doi:10.1016/j.surfcoat.2020.126537.